ADVANCED ENERGY MATERIALS
www.advenergymat.de

In Situ Built Nanoconfined TiO_2 Particles in Robust-Flexible MXene@rGO Conductive Framework Enabling High-Performance Hybrid Magnesium–Sulfur Batteries

Miao Guo, Chongyang Yuan, Tian Xu, Shulin Zhong, Wenbin Wang, Tongxin Zou, Tengfei Zhang, and Xuebin Yu**

The exploration of new and efficient sulfur cathodes through nanostructured materials design is vital for the development of high-performance metal–sulfur batteries, which is a promising candidate for next-generation energy storage systems. However, the shuttle behavior and sluggish reaction kinetics of polysulfides hinder the application of sulfur cathodes. Herein, a 3D MXene/reduced graphene oxide (rGO) composite conductive framework with superior specific surface area, structural stability, and ionic/electronic conductivity is constructed. On this basis, the TiO_2 nanoparticles, in situ grown in the interlayer between MXene and rGO can be used as adsorptive and catalytic active site for polysulfides to accelerate the electrochemical reaction kinetics and alleviate the shuttle effect, thereby improving cycle stability. Consequently, the sulfur-loaded MXene-TiO_2@rGO composite electrodes present a high reversible capacity of 1052.0 mAh g^{-1} at 0.2 C after 200 cycles, favorable high-rate capability, and splendid long-term performance, retaining 445.6 mAh g^{-1} capacity after 1000 cycles at 2 C in hybrid Mg/Li–S batteries. This work provides a new insight for using MXene as the sulfur host with high performance for metal–sulfur batteries.

1. Introduction

With the continuous development of energy technology, people gradually find that the rechargeable batteries system combined with sustainable energy and smart grid has great prospects in dealing with energy crisis and environmental pollution.[1] Metal–sulfur batteries based on multielectron conversion reactions are amongst the most promising candidates to satisfy emerging energy-storage demands, owing to their high theoretical capacity (1675 mAh g^{-1}), abundant reserves, low price, and eco-friendliness.[2] In terms of anode metal selection for metal–sulfur batteries, magnesium has gradually become a promising development direction in the post-lithium era due to its advantages of the high natural abundance in the crust (10^4 times that of lithium), high operating safety, dendrite-free deposition, and large volumetric capacity (3833 vs. 2062 mAh cm^{-3} for Li).[3] However, the inherent defect of Mg-based battery is Mg^{2+} with a bivalent nature is strongly affected by the electrostatic interaction of anions in the electrolyte, resulting in the strong solvation and slow ion migration in the electrolyte.[3b] Some recent studies prove that the reversibility of magnesium–sulfur batteries (MSBs) is improved by introducing lithium salt into the electrolyte. Both Mg^{2+} and Li^+ are involved in reaction of the conversion type cathodes (such as Co_9S_8, NiS, and S) during the charge–discharge process of magnesium–lithium hybrid batteries.[4] The fast diffusion kinetics of Li^+ accelerate the redox reaction of the sulfur cathode, while avoiding the dendrite problem of Li^+ deposition/dissolution at the anode (due to the lower redox potential of Li than Mg). The integration of high-safety Mg anode and fast sulfur cathode kinetics endow hybrid magnesium/lithium–sulfur batteries (MLSBs) a promising future.

Despite its great promise, the development of MLSBs has been hindered by several challenges.[5] First, both sulfur and its final reduction products (Li_2S/MgS) are electrical insulators, resulting in low utilization of active materials and poor electrochemical kinetics of cathodes. Second, long-chain polysulfides (Li_2S_n/MgS_n, $3 < n \leq 8$) which are the intermediate product of the conversion of S to Li_2S/MgS, can be dissolved in the electrolyte and penetrate the diaphragm to the negative electrode, resulting in anode corrosion and reduction of Coulombic efficiency (CE).[6] Finally, due to the volume expansion after the conversion of sulfur to MgS/Li_2S, the active materials fall off from the current collector, accelerating the decay of capacity.[2d]

A lot of explorations have been carried to solve these problems, and one of the main strategies is to design advanced sulfur host

M. Guo, C. Yuan, T. Xu, S. Zhong, W. Wang, T. Zou, X. Yu
Department of Materials Science
Fudan University
Shanghai 200433, P. R. China
E-mail: yuxuebin@fudan.edu.cn

T. Zhang
College of Materials Science and Technology
Nanjing University of Aeronautics and Astronautics
Nanjing 210016, P. R. China
E-mail: zhangtengfei@nuaa.edu.cn

The ORCID identification number(s) for the author(s) of this article can be found under https://doi.org/10.1002/aenm.202300417

DOI: 10.1002/aenm.202300417

materials for hybrid Mg/Li–S batteries (MLSBs) cathodes. Traditional carbon-based materials, such as porous carbon, carbon nanotubes, and graphene have high electron conductivity and specific surface area, which can improve the low conductivity of active materials. However, the weak intrinsic interaction between non-polar carbon and polar polysulfide intermediates leads to severe capacity attenuation during long-term cycling.[7] In comparison, the 2D transition metal carbide/carbonitride, viz., MXenes (such as Ti_2C and Ti_3C_2), not only has excellent inherent metallic conductivity and specific surface area, its polar Ti–C bond and surface hydrophilic groups can trap polysulfides through polar–polar interactions, thereby alleviating the shuttle effect while improving electrochemical reaction activity.[8] Nevertheless, MXene sheets are prone to restack due to Vander Waals interactions and hydrogen bonds, resulting in a decrease in specific surface area and hinders the ionic transport.[8a] Therefore, constructing the multi-dimensional structure or compositing with porous materials by MXene can solve the problem of sheet accumulation and volume expansion, thereby increasing the specific surface area and the structural stability of the cathode material. For example, Wagner and his team reported a porous MXene/CNT composite as a sulfur-loading matrix for MSBs.[9] The CNTs provide a high surface area and prevent MXene restacking, while polar surface groups of MXene can reduce polysulfide shuttling. Although the electrochemical capacity of the composite cathode is almost doubled, these materials still exhibit unsatisfied structure stability and limited active sites, leading to an unsatisfied cycle stability and sluggish redox kinetics.

To further improve the redox activity of MXene-based sulfur cathode, an effective strategy is to modify MXene with transition metal oxide, such as MnO_2, VO_2, Co_3O_4, and TiO_2. These metal oxides with high polarity reportedly provide a strong chemisorption and catalytic effect on the conversion of lithium polysulfides, which can effectively inhibit the "shuttle effect" and improve the redox reaction activity in lithium–sulfur batteries (LSBs).[10] Among them, TiO_2 has the advantages of high chemical stability, non-toxic, and strong redox ability. Despite these distinctive merits, the inferior electron conductivity (10^{-12} to 10^{-7} S cm^{-1}) of TiO_2 has restricted its efficient charge transfer upon cycling. In addition, unconfined TiO_2 particles with weak binding force to the substrate are easy to aggregate on the surface of MXene, resulting in uneven distribution on the surface and shedding during cycling.[8d,11] A reliable strategy to solve these problems is in situ oxidation of MXene to form nanosized TiO_2 particles and uniformly distribute on a conductive network, thereby increasing the specific surface area and ionic/electronic conductivity. On the other hand, in situ oxidation of MXene can remove the −F group on the surface of MXene which is unfavorable for the adsorption of polysulfides, further improving the efficiency of polysulfides capturing and catalytic conversion. On this basis, the uniform nanoconfined TiO_2 particles from in situ oxidation with a 3D MXene/carbon conductive matrix can be expected to be a stable and efficient sulfur host. This combination can not only improve the charge transport capacity of TiO_2 active site, but also physically limit the polysulfides within the interfacial interlayer, which effectively restrains the shuttling and achieves stable cycling. But so far, few researchers have put efforts to combine this oxide modification with 3D conductive framework construction on MXene-based materials for MLSBs, especially the function of TiO_2 has not been revealed in the magnesium polysulfides conversion process.

Here, we propose a method for in situ construction of TiO_2 nanoparticles on a robust-flexible composite conductive framework and apply in hybrid magnesium/lithium–sulfur batteries (MLSBs). As demonstrated in **Figure 1**, the 3D hollow nanosphere structure constructed by MXene with high structural strength can greatly increase the specific surface area of the material while alleviating structural damage caused by the volume change of sulfur during cycling, maintaining structural stability. Then, the rGO, with high structural flexibility, can crosslink MXene spheres like spider webs, which shorten the migration paths of electron/ion and reduces the migration energy barrier of Li^+/Mg^{2+}, thereby improving electrochemical kinetic and rate performance. More importantly, TiO_2 nanoparticles significantly enhance the adsorption/catalysis of polysulfides and confine them within the conductive framework, thus mitigating the "shuttle effect" and improving cycle stability. As a result, the spheroidal-MXene-TiO_2@rGO-S electrode delivers a reversible capacity of 1052.0 mAh g^{-1} at 0.2 C after 200 cycles and shows excellent cycle performance (a reversible capacity of 445.6 mAh g^{-1} at 2 C after 1000 cycles with a low degradation rate of 0.016% per cycle) in MLSBs, which is one of the best performances for MLSBs batteries reported to date, demonstrating its great potential for implementation in next-generation high-performance post lithium-ion batteries.

2. Results and Discussion

2.1. Preparation and Structural Analysis of Materials

Figure S1 (Supporting Information) shows a detailed schematic process for preparing sulfur-loading spherical MXene, spherical MXene@rGO, and spherical MXene-TiO_2@rGO, denoted as *s*-MX-S, *s*-MX@rGO-S, and *s*-MXTO@rGO-S, respectively. The X-ray diffraction (XRD) patterns of as-prepared and sulfide samples are displayed in **Figure 2**a and Figure S2a (Supporting Information). The XRD patterns of MXene and GO precursor agree with the simulated patterns of reported crystal structures.[12] The *s*-MX@rGO composite material shows characteristic peaks of MXene and rGO, which proves that GO is reduced to rGO and well compounded with MXene (Figure 2a). After oxidation treatment, the diffraction peak at ≈27.5° can be ascribed to the lattice plane of (110) of rutile TiO_2, indicating that partial Ti atoms on MXene's surface have been in situ transformed into TiO_2 giving the target *s*-MXTO@rGO composites. The characteristic peaks of sulfur are observable after sulfur filling, indicating a successful impregnation of sulfur into the host (Figure 2b). The Brunauer–Emmett–Teller (BET) surface areas of composites and *f*-MX were evaluated by N_2 adsorption–desorption tests. As shown in Figure 2c, the BET surface area of *s*-MX (98.96 cm^2 g^{-1}) is nearly ten times that of the *f*-MX (9.48 cm^2 g^{-1}), which proves that the construction of 3D conductive framework can effectively prevent *f*-MX from restacking, thereby increasing the specific surface area. Due to the lower volume density of rGO, the specific surface area of the MXene sphere is increased after combination with rGO. After oxidation treatment, the specific surface area of the material further increases (from 106.45 to 136.91 cm^2 g^{-1}). Some literatures have shown that TiO_2 produced by in situ oxidation will form

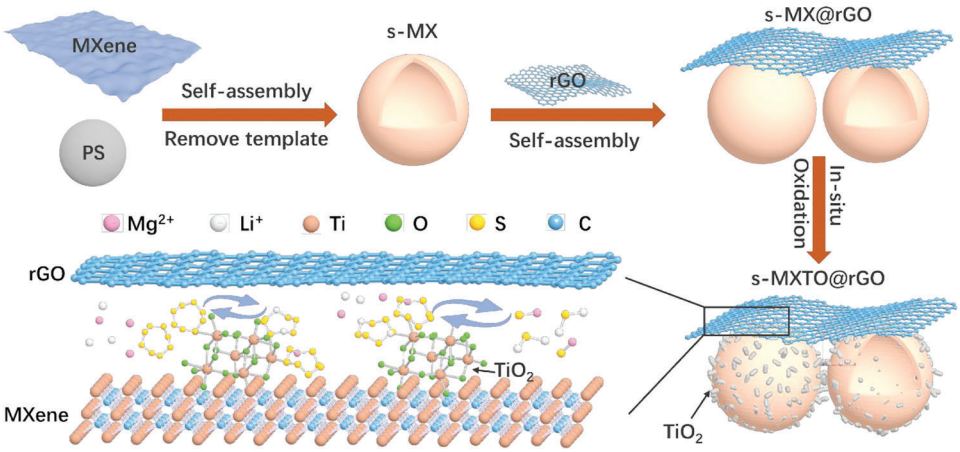

Figure 1. Schematic illustration of the fabrication for spheroidal MXene-TiO_2@rGO composite and the function of the spheroidal MXene-TiO_2@rGO heterostructure in MLSBs.

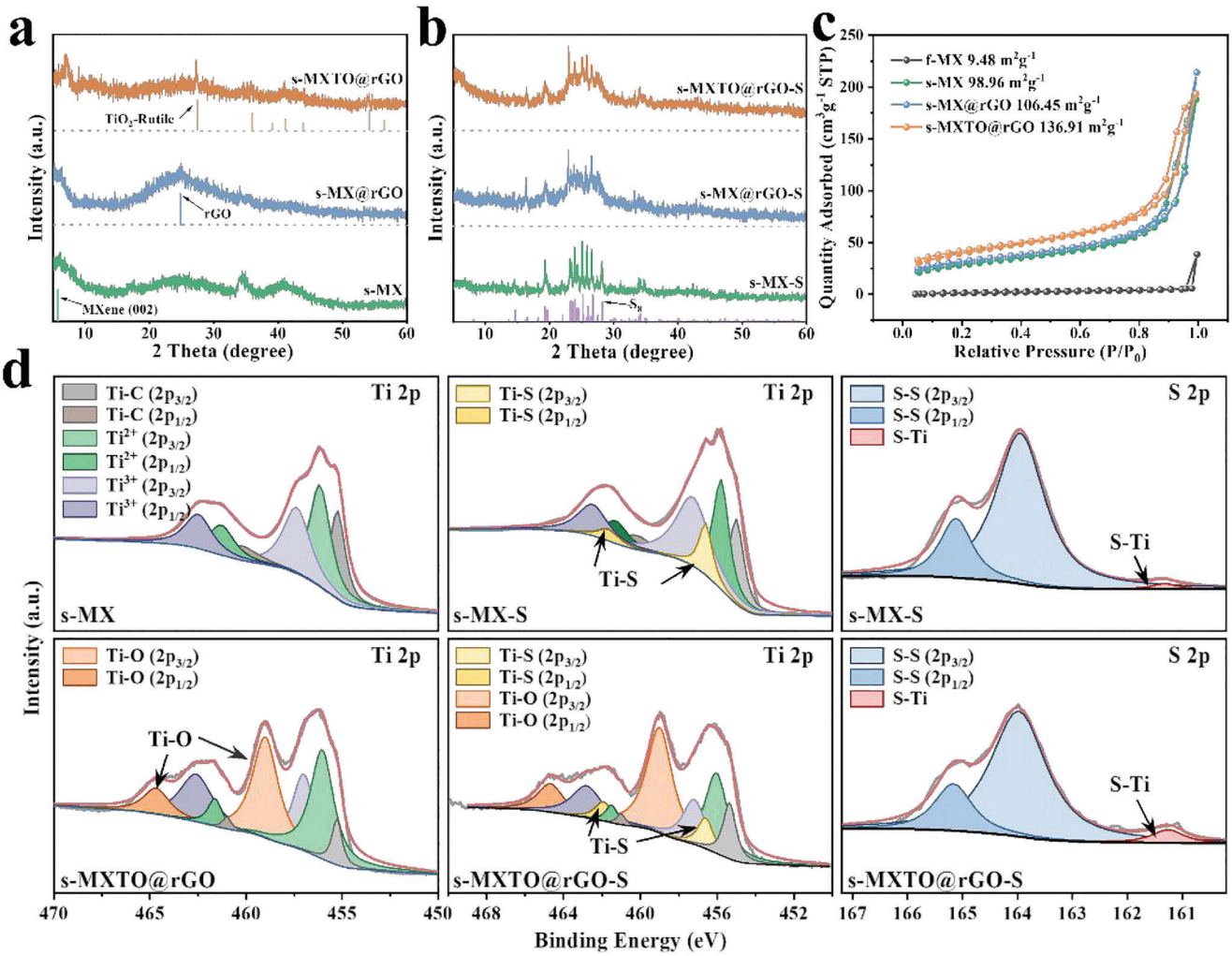

Figure 2. a) XRD patterns of *s*-MX, *s*-MX@rGO, and *s*-MXTO@rGO. b) XRD patterns of *s*-MX-S, *s*-MX@rGO-S, and *s*-MXTO@rGO-S. c) N_2 adsorption–desorption isotherms of the *f*-MX, *s*-MX, *s*-MX@rGO, and *s*-MXTO@rGO composite. d) XPS spectra at high resolution of Ti 2*p* and S 2*p* of *s*-MX, *s*-MX-S, *s*-MXTO@rGO, and *s*-MXTO@rGO-S materials.

micropores and mesopores on the surface of MXene.[11,13] These pores connect the hollow spheres inside and outside, thereby increasing the specific surface area of the material. To obtain the true content of sulfur in *s*-MX-S, *s*-MX@rGO-S, and *s*-MXTO@rGO-S composite materials, the TGA tests were performed on the materials after loading sulfur. The contents of S in the *s*-MX-S, *s*-MX@rGO-S, and *s*-MXTO@rGO-S cathode materials for MLSBs are 29.1, 30.3, and 28.5 wt.%, respectively (Figure S2b, Supporting Information). In addition, *s*-MXTO@rGO-S with 53.21 and 69.79 wt.% sulfur-loadings are named as *s*-MXTO@rGO-S-50 and *s*-MXTO@rGO-S-70 wt.%, respectively, and used to explore the possibility of high sulfur-loading MLSBs (Figure S2c, Supporting Information).

The surface element composition and chemical valence of the three samples were characterized by X-ray photoelectron spectroscopy (XPS) measurement as illustrated in Figure 2d and Figure S2 (Supporting Information), demonstrating the characteristic peaks of Ti, F, O, C, and Cl in the survey spectra of the *s*-MX, *s*-MX@rGO, and *s*-MXTO@rGO. After combining with rGO, the strength of F peak is greatly weakened, and the C peak is enhanced. To clarify the chemical state of these elements, Ti 2*p*, C 1*s*, and S 2*p* spectra were further investigated. The high-resolution Ti 2*p* spectrum of *s*-MX can be deconvoluted into six peaks at the binding energy of 455.22 (461.09), 456.12 (461.99), and 457.17 (463.04) eV, corresponding to Ti–C 2*p*3/2 (2*p*1/2), Ti^{2+} 2*p*3/2 (2*p*1/2), and Ti^{3+} 2*p*3/2 (2*p*1/2), respectively. After compounding and oxidation, the relative intensity of Ti^{2+} and Ti^{3+} peaks decrease, but two peaks appear at 458.62 and 464.68 eV, corresponding to Ti–O 2*p*3/2 and 2*p*1/2, respectively, which further prove the in situ generation of TiO_2 particles.[14] After sulfur filling, Ti–S peaks appear at 456.60 and 461.92 eV in the Ti 2*p* spectrum, indicating the certain chemical absorption of sulfur through the Ti atoms on the MXene surface. It is noted that the S–Ti peak (161.27 eV) of *s*-MXTO@rGO-S is obviously stronger than that of the *s*-MX-S in the S 2*p* fine spectra, which suggest that in situ TiO_2 can further strengthen the chemical adsorption of sulfur through Ti–S bond.

SEM and TEM were used to characterize the nanostructure and morphology of the whole material preparation process step by step as shown in **Figure 3** and Figures S3–S5 (Supporting Information). MXene sheets are uniformly coated on polystyrene (PS) nanospheres by electrostatic adsorption (Figure S3c, Supporting Information), and the composite of GO further strengthens the cross-linking between PS@MXene spheres, forming the PS@MX@GO composite structure (Figure S3d, Supporting Information). After calcination, all three samples show a hollow spherical shape with a particle size of 270–300 nm (Figure S4a1–c1,a2–c2, Supporting Information). After in situ oxidation reaction, massive nano-particles ≈20–30 nm appear between the interlayer between MXene and rGO in the *s*-MXTO@rGO sample (Figure S4c3, Supporting Information). The energy-dispersive X-ray spectroscopy (EDS) mapping results show that the Ti and O elements aggregate and distribute in the particles (Figure 3c4; Figure S4c4, Supporting Information). Moreover, the measured *d*-spacing of 2.49 Å in the high-resolution TEM (HRTEM) image (Figure 3c3) corresponds to the (101) lattice plane of rutile-type TiO_2, which is consistent with the above results of XRD phase structure analysis and EDS elemental analysis. The hollow spherical morphology of the three samples remains intact after calcination and sulfur-loading, and no sulfur aggregation occurs on the samples, indicating that 3D conductive frame has sufficient specific surface area and structural strength to support sulfur (Figure 3a1–c1,a2–c2). On the contrary, the spheroidal rGO (*s*-rGO) partially maintain the spherical shape after calcination, loading sulfur will lead to the collapse of the hollow spheres and damage the structure (Figure S5, Supporting Information). Significantly, as presented in Figure 3a3–c3,c4, S is homogeneously loaded on the surface of the hollow sphere and exhibits a concentrated distribution around TiO_2 particles.

2.2. Electrochemical Performance and Kinetics Analysis for MLSBs

To further investigate the influence of conductive framework and TiO_2 active sites on Mg^{2+}/Li^+ storage performance, the *s*-MX-S, *s*-MX@rGO-S, and *s*-MXTO@rGO-S composites were evaluated as cathode materials coupled with APC-LiCl electrolyte, Mg foil anode, copper foam, and glass fiber separator in coin cells of MLSBs. **Figure 4**a presents the cyclic voltammetry (CV) curves of the first three cycles at a sweep rate of 0.2 mV s^{-1} in the voltage range of 0.1–1.7 V versus Mg^{2+}/Mg. Three peaks are observed at 1.54, 1.05, and 0.91 V during the first discharge process. Subsequently, the peaks position progressively move toward a higher voltage (such as from 0.91 to 0.94 V) during the following cathodic scans, indicating the decreased polarization. The peak at 1.54 V could be attributed to the transformation of sulfur into long-chain polysulfides (MgS_n, $3 < n \leq 8$), and the low-voltage peak (1.05 and 0.91 V) should be attributed to the formation of shot-chain polysulfides (MgS_n, $n \leq 3$). However, since lithium polysulfide redox reaction take place at similar potential, it is like that Mg/Li polysulfide may also form due to Li^+ incorporation into magnesium polysulfide at this potential domain.[4a] Among the three samples, *s*-MXTO@rGO-S exhibits higher current response and smaller redox potential gaps, demonstrating its better reaction activity toward Mg/Li–S conversions. The overlaps of the second and third curves are different from *s*-MX-S and *s*-MX@rGO-S, which further illustrates the better cycle stability of the *s*-MXTO@rGO-S cathode than the other two samples (Figure 4a; Figure S6, Supporting Information). The galvanostatic charge–discharge voltage profiles of electrodes evaluated at a current density of 0.2 C within a voltage of 0.1–1.7 V are shown in Figure S7 (Supporting Information). The charge–discharge platform of the *s*-MXTO@rGO-S electrode is more evident than that of the *s*-MX-S and *s*-MX@rGO-S, indicating a more apparent conversion reaction activity and the reversibility, which coincides well with the CV results. The improvement of its performance may be due to the promotion of ion/electron transport by the composite conductive framework, which is proved by EIS impedance test. The EIS spectra of cathodes show semicircles in the high frequency region and sloping lines in the low frequency region, which correspond to charge transfer resistance (R_{ct}) at the electrode/electrolyte interface and the Mg^{2+}/Li^+ diffusion resistance within electrode materials, respectively. The composite conductive frameworks formed by crosslinking of rGO and MXene hollow spheres accelerate the diffusion and transfer of electrons and ions, which are weighted in favor of reaction kinetics

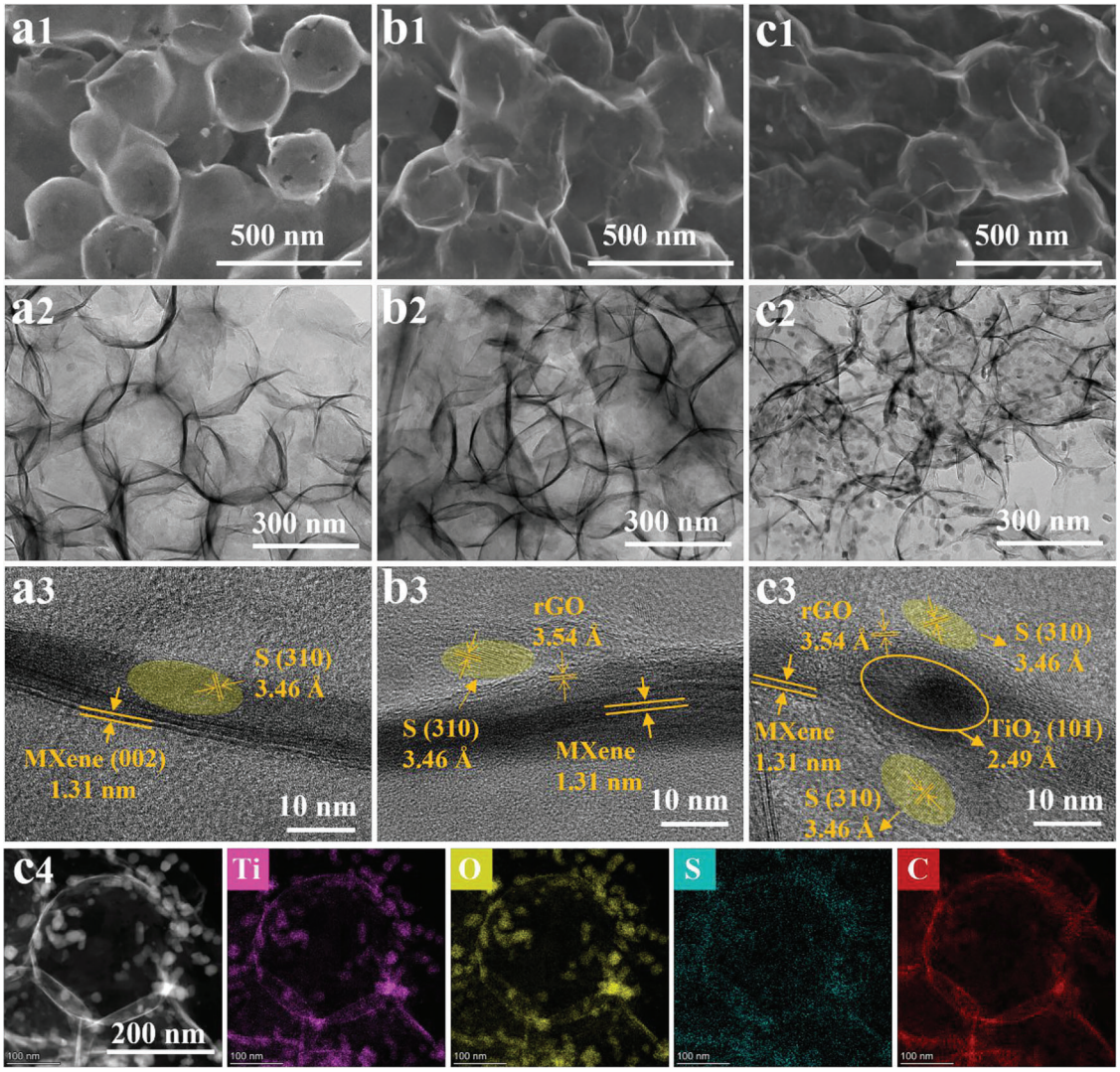

Figure 3. a1–c1) SEM images, a2–c2) TEM images, a3–c3) HRTEM images for *s*-MX-S, *s*-MX@rGO-S, and *s*-MXTO@rGO-S, respectively. c4) TEM images and corresponding elemental mappings of Ti, O, S, and C for *s*-MXTO@rGO-S.

and rate performance. After oxidation, the conductivity decreases slightly due to the low conductivity of TiO_2.

Thereafter, the cycle stability and rate performance of *s*-MX-S, *s*-MX@rGO-S, and *s*-MXTO@rGO-S electrodes were elucidated. Notably, the specific capacities are calculated according to the mass of active S in the composite materials (≈0.5 mg cm^{-2}). Figure 4c shows the cycle curves and CE of *s*-MX-S, *s*-MX@rGO-S, and *s*-MXTO@rGO-S electrodes at a current of 0.2 C. The capacity retention of *s*-MXTO@rGO-S after 200 cycles is 1052.0 mAh g^{-1}, which is much higher than that of *s*-MX-S (282.3 mAh g^{-1}) and *s*-MX@rGO-S (416.1 mAh g^{-1}). The CE of *s*-MX-S and *s*-MX@rGO-S samples gradually increased from 55% to 100% in the first 30 cycles. The *s*-MXTO@rGO-S cathodes exhibit a high charge/discharge capacity (1151.7/1735.7 mAh g^{-1}) in the first cycle with a CE of 66.35%. Interestingly, unlike the other two samples, the CE of *s*-MXTO@rGO-S cathode sample reaches 109.20% in the second cycle and increases to 114% in the 7th cycle, and then gradually stabilizes ≈100% in the next 40 cycles. The reason for this difference may be that TiO_2 active sites can inhibit of shuttle effect and promote the conversion reaction of polysulfide, thus increasing the charging capacity. In addition, the capacity contributed by the decomposition of the electrolyte during high-voltage charging also leads to the CE >100%. With the decrease of sulfur and polysulfide concentration in the electrolyte, this catalytic effect gradually weakens, reaching a certain balance and stabilizing the CE at ≈100%. Figure 4e compares their rate performance. As expected, *s*-MXTO@rGO-S delivers the highest capacities of 1057.8, 741.4, 590.4, 473.9, and 299.2 mAh g^{-1} at current densities of 0.2, 0.5, 1, 2, and 5 C, respectively. When the current density returns to 0.2 C, the capacity immediately returns to 917.3 mAh g^{-1} immediately, suggesting good tolerance and excellent cycle stability. Although the electrochemical capacity of *s*-MX@rGO-S is relatively low, it shows good rate performance, which further proves that the composite conductive framework of rGO and MXene can improve ion/electron conduction, leading to faster kinetics reaction and

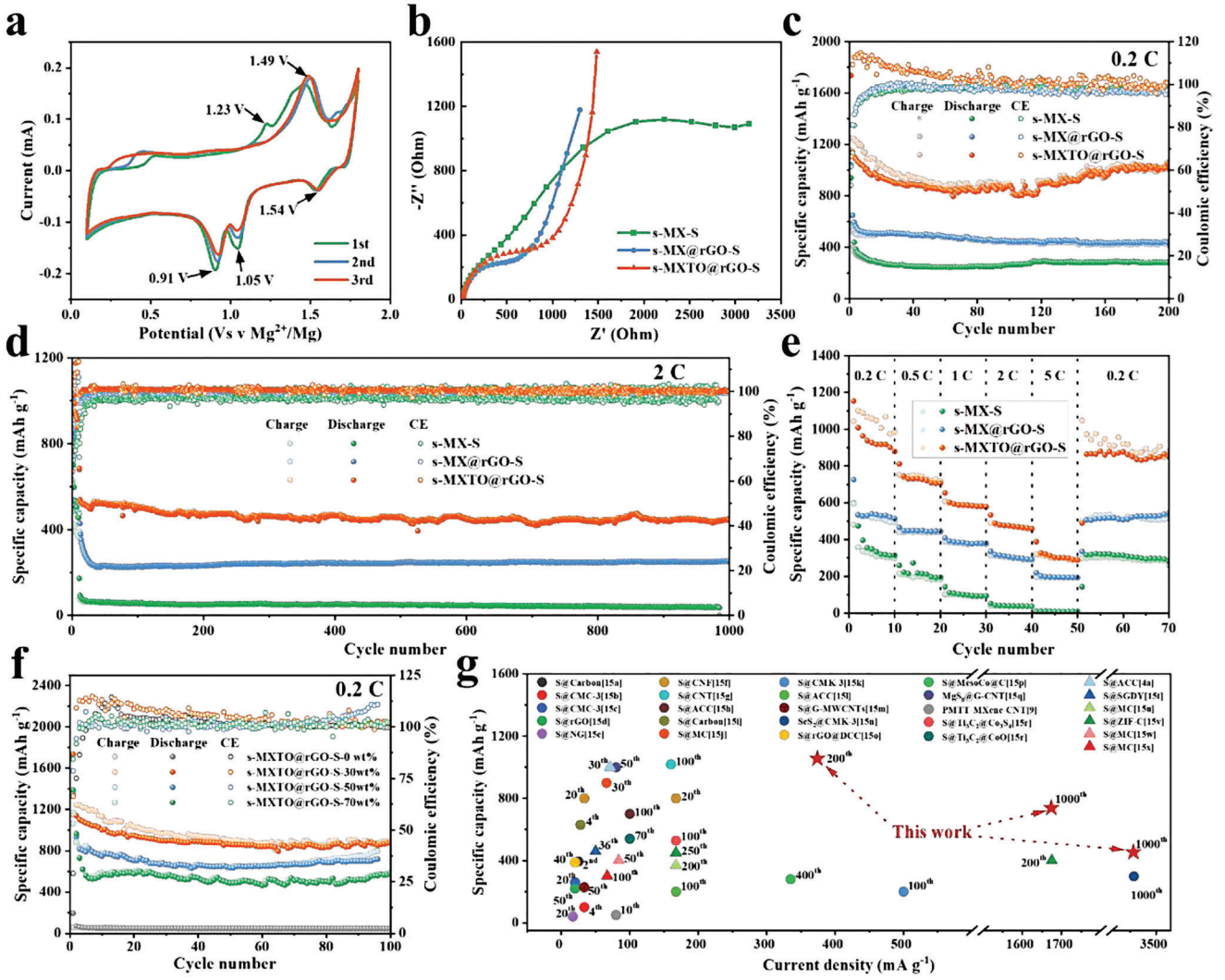

Figure 4. Electrochemical performances of *s*-MX-S, *s*-MX@rGO-S, and *s*-MXTO@rGO-S for MLSBs. a) The CV curves of *s*-MXTO@rGO-S at 0.2 mV s^{-1}. b) Nyquist plots of *s*-MX-S, *s*-MX@rGO-S, and *s*-MXTO@rGO-S before cycling. c) Cycling performance of *s*-MX-S, *s*-MX@rGO-S, and *s*-MXTO@rGO-S at 0.2 C. d) Long-term cyclability of *s*-MX-S, *s*-MX@rGO-S, and *s*-MXTO@rGO-S at 2 C. e) Rate capabilities of three electrodes at various current densities. f) Cycling performance of *s*-MXTO@rGO-S with different sulfur-loading at 0.2 C. g) Comparison of rate capability of the state-of-the-art cathodes for reported MSBs (circular marks) and MLSBs (triangle marks).

superior rate capability. To determine the favorable long-term cyclability, the composite cathodes were measured at a high current density of 2 C (Figure 4d). A high reversible capacity of 445.6 mAh g^{-1} is delivered >1000 cycles with a low degradation rate of 0.016% per cycle, displaying a CE stabilized at ≈100% during the long-term cycling. As shown in Figure 4f, the cycle stabilities of *s*-MXTO@rGO-S electrodes with different sulfur-loading were also tested. Sulfur-free samples contribute little capacity during cycling, and the 70 wt.% sulfur-loaded *s*-MXTO@rGO electrode has a capacity of 583.2 mAh g^{-1} at 0.2 C after 100 cycles. Compared to previously reported sulfur-based cathodes for MSBs and MLSBs (Figure 4g and Table S1, Supporting Information), the *s*-MX@rGO-S electrode is highly competitive in capacity output, cycle stability, and rate performance.[4a,9,15]

To gain insights into the origin of the improved electrochemical performance after the construction of the conductive frameworks and TiO_2 active site, CV and galvanostatic intermittent titration technique (GITT) measurements were performed to analyze the kinetics. As shown in **Figure 5**a, similar cathodic and anodic current responses in CV tests are recorded at sweep rates ranging from 0.2 to 1 mV s^{-1}, and there is no obvious shift of the location of the oxidation peak, indicating the fast kinetics and small polarization.[16] The slopes of the log(*v*)–log(*i*) plots at the anodic peak at 1.49 V and at the cathodic peaks at 0.91 V are ≈0.74 and 0.55, suggesting a mixture of capacitive and diffusion-controlled process (Figure 5b). To quantify the contribution of diffusion-limited and capacitive behaviors at a certain scan, the ratios of non-diffusion-limited charge storage was calculated. The ratios of capacitive contribution gradually increase with the increase of sweep rate (Figure 5d). The capacitive contribution of the *s*-MXTO@rGO-S electrode at 1.0 mV s^{-1} was 76% as shown by the orange area, which is lower than that of *s*-MX@rGO-S

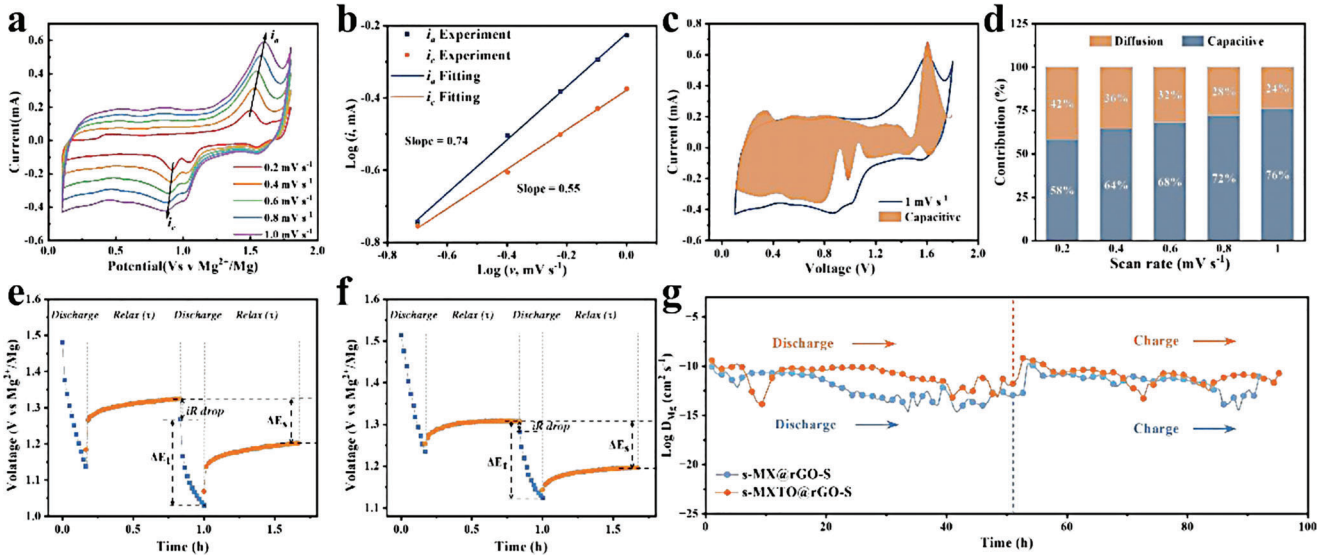

Figure 5. Electrochemical kinetics analysis of the *s*-MXTO@rGO-S for MLSBs. a) CV curves at different scan rates from 0.2 to 1 mV s^{-1}. b) *b*-value analysis through the relation of the peak current (*i*) and the scan rate (*v*). c) Capacitive contribution area (orange) at the 1.0 mV s^{-1}. d) Capacitive contribution ratios at 0.2–1 mV s^{-1}. e) An enlarged view of *s*-MX@rGO-S electrode potential during a GITT pulse for the MLSBs. f) An enlarged view of *s*-MXTO@rGO-S electrode potential during a GITT pulse for the MLSBs. g) The calculated chemical diffusion coefficient for Mg-ion in the *s*-MX@rGO-S and *s*-MXTO@rGO-S cathodes versus cycle time.

electrode (Figure 5c; Figure S10, Supporting Information). Therefore, it can be speculated that the increase of the electrochemical capacity of *s*-MXTO@rGO-S compared with sample *s*-MX@rGO-S may come from the faradaic charge-storage process catalyzed by TiO_2 adsorption sites.

In addition, the variation in Mg^{2+}/Li^+ solid-state diffusion during charge and discharge process was employed by GITT. Based on the potential response with time (Figure S11, Supporting Information), the calculated ion diffusion co-efficient (D_{GITT}) of electrodes during the 10th discharge/charge are given in Figure 5g. And Figure 5e,f displays two GITT steps of the *s*-MX@rGO-S and *s*-MXTO@rGO-S cathodes in terms of discharge, respectively. Compared with the *s*-MX-S electrode, the D_{GITT} value of the *s*-MX@rGO-S electrode raises by one magnitude, indicating that the composite of rGO can accelerate the ionic migration (Figure 5g; Figure S12, Supporting Information). The GITT curves of *s*-MX@rGO-S and *s*-MXTO@rGO-S cathode samples are close because of the similar composite conductive frames, but the D_{GITT} of *s*-MXTO@rGO-S is higher, which can ascribe to larger specific surface area and more active sites.

To better understand Mg^{2+}/Li^+ storage behavior, the reaction mechanisms were investigated via ex situ XRD, XPS, TEM, and selected area electron diffraction (SAED) technologies. **Figure 6**a provides the initial charge–discharge curves of *s*-MXTO@rGO-S for MLSBs and corresponding sites to be probed by ex situ XRD (Figure 6b). With regard to the XRD pattern of pristine *s*-MXTO@rGO-S (point A), there are four distinct diffraction peaks at 37.7°, 46.5°, 48.6°, and 54.2° attributed to Cu_2S (JCPDS no. 26-1116). Some reports show that copper foam can not only play chemical and physical adsorption on polysulfides, but also transform with S_8 molecules and polysulfides to produce Cu_2S or CuS in the electrolyte containing Cl^- and polysulfides, which explains the source of Cu_2S in the original material.[15n,u,17] As the increase of discharge degree, the diffraction peak of Cu_2S first increases, then decreases until it disappears. The diffraction peak of Cu (JCPDS no. 89-2838) appears at 43.3° and 50.4° when the discharge potential reached to 1 V. As the discharge degree increase, the diffraction peak of Cu gradually increased, and then decreased obviously at the subsequent charging stage. It indicates that the Cu in the positive electrode system has undergone a Cu–Cu_2S–Cu transformation during the whole discharge process, which plays a catalytic role and make few contributions to capacity. More significantly, weak peaks at 44.8° and 49.5° can be identified as characteristic peaks of Li_2S (JCPDS no. 26-1188) and MgS (JCPDS no. 35-0730). It confirms that both Mg^{2+} and Li^+ are involved in the positive reaction in the dual-salt electrolyte.

To further investigate redox reactions during discharge/charge, *s*-MXTO@rGO-S cathodes were examined by XPS. Figure 6c displays the high-resolution XPS spectra of Mg 2*p* and Li 1*s* of the cathodes at first discharge to 0.1 V. The results showed that Li_2S and MgS appear in the discharge products, indicating that both Mg^{2+} and Li^+ in the electrolyte participate in the reaction in MLSBs. The Li 1*s* spectra of *s*-MX-S exhibit one signal at 53.2 eV, attributable to the pillared Li^+ species. The pillared Li^+ is embedded between the layers of the lamellar structure and plays a role in expanding the layer spacing.[4c] However, it has a very strong binding force with the lamellar structure and is not easy to come out, which will lead to the occurrence of the side reaction of the electrolyte and the decrease of the CE. In addition, comparing the three samples, the peak intensity ratio of MgS and Li_2S in the discharge product increases from 0.68 (*s*-MX-S) to 1.08 (*s*-MXTO@rGO-S). It is suggested that that the composite conductive framework and TiO_2 active sites can specifically improve the reactivity of magnesium polysulfide, which also explains the high electrochemical capacity of the sample.

TEM analysis was also carried out to determine the morphology of the cathode material and the phase composition of the fully

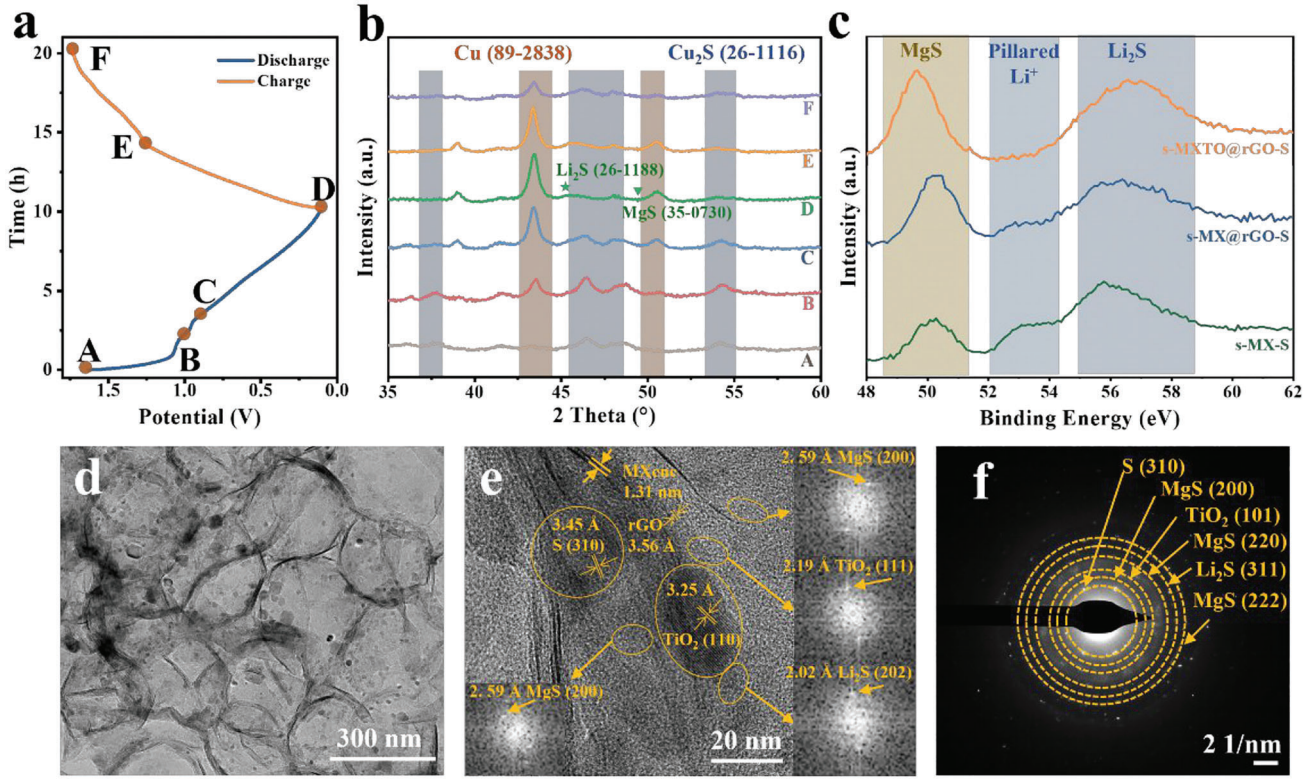

Figure 6. a) The voltage–time curve of *s*-MXTO@rGO-S cathode in various states (A–F) during first cycle and b) corresponding ex situ XRD patterns. c) The XPS spectra of Mg 2*p* and Li 1s at first discharge to 0.1 V for *s*-MX-S, *s*-MX@rGO-S, and *s*-MXTO@rGO-S. d) The TEM, e) HRTEM, and f) SEAD images of full-discharge *s*-MXTO@rGO-S electrode after 50 cycles at 0.2 C current.

discharged product after 50 cycles at 0.2 C current. It can be seen from Figure 6d that the sample still maintains a complete hollow sphere structure, and there is no obvious aggregation of discharge products on the surface after 50 cycles. It demonstrates that the superior structural strength of MXene can mitigate structural damage caused by the volume change of S during charging and discharging, while the hollow sphere has a large specific surface area and provides sufficient reaction surface for polysulfides. The HRTEM and SAED of fully discharged *s*-MXTO@rGO-S depicted in Figure 6e,f adequately testify the generation of Li_2S and MgS. These products tend to aggregate around TiO_2 particles, which also confirms the adsorption and catalytic reaction of TiO_2 on polysulfides.

Based on the above analyses and the previous reports on CuS and Cu_2S, the *s*-MXTO@rGO-S electrode reaction during the discharge process in MLSBs is summarized as follows steps.[17,18] First, as shown in Equations 1 and 2, part of S_8 in the original material dissolves in the ether electrolyte to form S_8^{2-}. It reacts with copper foam to form Cu_2S attached to the surface of the sample, which explains the diffraction peak of Cu_2S shown in the original sample in XRD patterns.

$$S_8 + 2e^- \rightarrow S_8^{2-} \quad (1)$$

$$S_8^{2-} + 16Cu \rightarrow 8Cu_2S + 2e^- \quad (2)$$

As the discharge proceeds, S_8 reacts with Li^+ and Mg^{2+} to form soluble polysulfides (such as MgS_8, MgS_4, Li_2S_8, and Li_2S_4). These discharge products further react with Cu to form Cu_2S, MgS, and Li_2S (Equations 3 and 4).

$$(0.5x + y)\,S_8 + xLi^+ + yMg^{2+} + (x + 2y)e^- \rightarrow 0.5xLi_2S_8 + yMgS_8 \quad (3)$$

$$0.5xLi_2S_8 + yMgS_8 + (7x + 14y)\,Cu \rightarrow (3.5x + 7y)\,Cu_2S + 0.5xLi_2S + yMgS \quad (4)$$

Finally, Cu_2S produced in Equations 2 and 4 further reacts with Mg^{2+} and Li^+ in the electrolyte to form Cu, MgS, and Li_2S (Equation 5).

$$(0.5x + y)\,Cu_2S + xLi^+ + yMg^{2+} + (x + 2y)\,e^- \rightarrow 0.5xLi_2S + yMgS + (x + 2y)\,Cu \quad (5)$$

In conclusion, copper foam can catalyze the formation of Li_2S and MgS by reacting with S_8 and polysulfide to form Cu_2S in the cathode reaction. And the composite conductive framework and TiO_2 active sites further adsorb and catalyze the conversion of polysulfides, thereby further improving their electrochemical reaction activity and cycle stability.

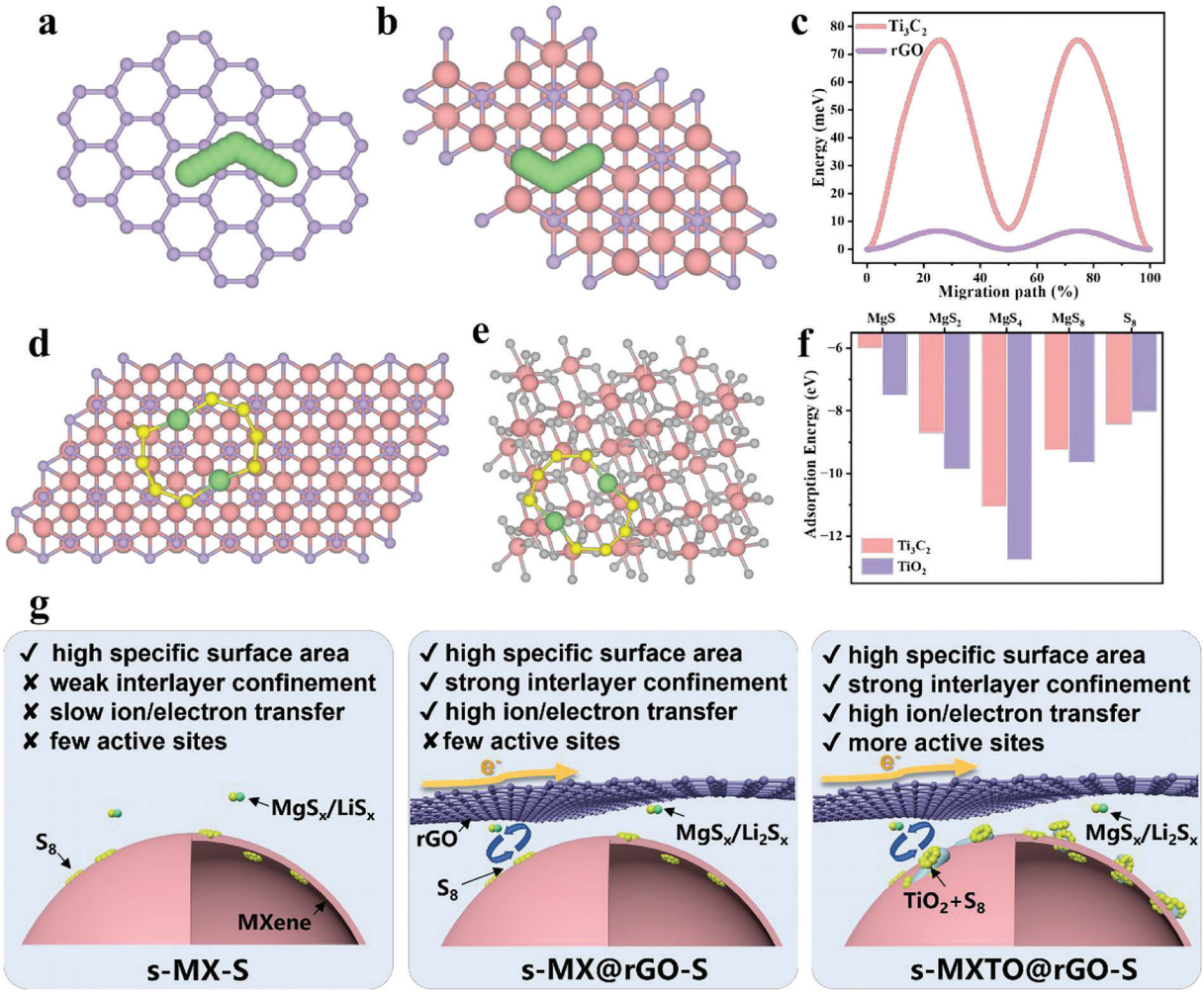

Figure 7. The simulated migration pathway of Mg^{2+} on a) rGO and b) Ti_3C_2. c) Corresponding calculated energy profile. Optimized configurations of MgS_4 (Mg_2S_8) absorption on d) Ti_3C_2 and e) TiO_2 (110) facet (Ti: pink; C: purple; O: gray; Mg: green; and S: yellow). f) Corresponding calculated Mg^{2+} adsorption results. g) Schematic diagram of performance improvement mechanism of the *s*-MX, *s*-MX@rGO, and *s*-MXTO@rGO-S electrodes for MLSBs.

2.3. Theoretical Calculations

To further explore the improvement mechanism of the composite conductive framework and TiO_2 nanoparticle, density functional theory (DFT) was used to simulate Mg^{2+} migration and the MgS_x ($1 \leq x \leq 8$) adsorption/decomposition differences between different samples. As shown in **Figure 7**a–c, Mg^{2+} migration pathways on rGO and Ti_3C_2 (MXene) are inscribed. The migration energy barriers are calculated to be 75 and 6.6 meV for MXene and rGO, respectively, demonstrating the composition of rGO can supply smoother Mg^{2+} diffusion and transfer for fast reaction kinetics in MLSBs. The same ameliorative Li^+ diffusion is also observed in Figure S14 (Supporting Information). In addition, Figure 7d–f exhibits the calculated adsorption energy (E_{ads}) between TiO_2 and MgS_4 (Mg_2S_8) is −12.7 eV, lower than that between Ti_3C_2 and MgS_4 (−11.0 eV). As for MgS_8 and MgS, the calculated E_{ads} of TiO_2 are −9.6 and −7.5, respectively, lower than that of Ti_3C_2. The stronger adsorption of magnesium polysulfide by TiO_2 leads to a more effective suppression of the shuttle effect for TiO_2 anchoring on Ti_3C_2 than that for Ti_3C_2 alone, hence favoring better cycling behavior in MLSBs. Figure S16 (Supporting Information) also shows that the calculated E_{ads} between lithium polysulfide with TiO_2 is lower than that of Ti_3C_2, obviously indicating the effective inhibitory shuttle effect for TiO_2 anchoring on Ti_3C_2. Moreover, bond-breaking process of MgS_2 decomposition into MgS on the surface of MXene and TiO_2 were simulated by DFT calculation (Figure S17, Supporting Information). The calculation results show that TiO_2 could disperse the positive charge of Mg^{2+} cations by forming the O–Mg interaction, thus reducing the bond-breaking barrier of Mg–S, to achieve the effect of catalytic reaction.

Figure 7g summarizes the mechanism of performance improvement. By constructing MXene with large structural strength into a 3D hollow sphere structure, the destructive effect of the volume change of sulfur on the structure during cycling can be effectively alleviated, while reducing the stacking of the sheets and increasing the specific surface area of the electrode material. After the composition of rGO, the electron/ion conductivity

of the cathode is improved, thereby accelerating electrochemical kinetics, and improving rate performance. Further in situ generation of TiO_2 nanoparticles inhibits the shuttle effect and catalyzes the conversion reaction by adsorbing and confining polysulfides within the interlayers of MXene and rGO, thereby increasing electrochemical capacity and improving cycle stability. Therefore, the *s*-MXTO@rGO with a high specific surface area, superior ion/electron conduction and abundant active sites enables outstanding performance in MLSBs.

3. Conclusion

In summary, we have designed and synthesized a 3D robust-flexible MXene/rGO composite conductive framework with in situ generated TiO_2 nanoparticles. The composite materials are employed as sulfur hosts in MLSBs to systematically investigate the synergistic effect of conductive frameworks and TiO_2 active sites on magnesium polysulfides redox reaction process. The experimental results combine with theoretical calculations show that the MXene/rGO composite conductive framework increases the specific surface area and accelerates electron/ion conduction, thereby improving the electrochemical reaction rate. At the same time, the nanoconfined TiO_2 particles within the interface of MXene/rGO can provide active sites for adsorption and reaction for the transformation of S and polysulfides, alleviate the shuttle effect, and greatly improve the utilization of active substances. Therefore, the *s*-MXTO@rGO cathode delivers a high reversible capacity of 1052.0 mAh g^{-1} at 0.2 C after 200 cycles and superb cycle stability (445.6 mAh g^{-1} after 1000 cycles at 2 C), demonstrating its great potential for MLSBs. Our strategy can be extended to other 2D materials to construct composite conductive frameworks and offer some thoughts for generating confined active sites to adsorb and catalytic polysulfides toward metal sulfur batteries.

Supporting Information

Supporting Information is available from the Wiley Online Library or from the author.

Acknowledgements

M.G. and C.Y. contributed equally to this work. This work was supported by the National Natural Science Foundation of China (51971065, 52171180, and 51802154), the Innovation Program of Shanghai Municipal Education Commission (2019-01-07-00-07-E00028), and the Fundamental Research Funds for the Central Universities (NG2022005).

Conflict of Interest

The authors declare no conflict of interest.

Data Availability Statement

The data that support the findings of this study are available from the corresponding author upon reasonable request.

Keywords

3D conductive frameworks, magnesium–sulfur batteries, MXene, rGO, TiO_2 active sites

Received: February 8, 2023
Revised: March 24, 2023
Published online:

[1] D. Larcher, J. M. Tarascon, *Nat. Chem.* **2015**, *7*, 19.
[2] a) S. H. Chung, A. Manthiram, *Adv. Mater.* **2019**, *31*, 1901125; b) X. Yu, A. Manthiram, *Adv. Funct. Mater.* **2020**, *30*, 2004084; c) L. Medenbach, P. Adelhelm, *Top. Curr. Chem.* **2017**, *375*, 81; d) X. Liu, Y. Li, X. Xu, L. Zhou, L. Q. Mai, *J. Energy Chem.* **2021**, *61*, 104.
[3] a) L. Kong, C. Yan, J.-Q. Huang, M.-Q. Zhao, M.-M. Titirici, R. Xiang, Q. Zhang, *Energy Environ. Mater.* **2018**, *1*, 100; b) G. Bieker, V. Küpers, M. Kolek, M. Winter, *Commun. Mater.* **2021**, *2*, 37.
[4] a) T. Gao, M. Noked, A. J. Pearse, E. Gillette, X. Fan, Y. Zhu, C. Luo, L. Suo, M. A. Schroeder, K. Xu, S. B. Lee, G. W. Rubloff, C. Wang, *J. Am. Chem. Soc.* **2015**, *137*, 12388; b) T. Li, A. Qin, H. Wang, M. Wu, Y. Zhang, Y. Zhang, D. Zhang, F. Xu, *Electrochim. Acta* **2018**, *263*, 168; c) H. Xu, X. Zhang, T. Xie, Z. Li, F. Z. Sun, N. Zhang, H. Y. Chen, Y. X. Zhu, X. S. Zou, C. Lu, J. X. Zou, R. M. Laine, *Energy Storage Mater.* **2022**, *46*, 583; d) G. Zhu, G. Xia, H. Pan, X. Yu, *Adv. Sci.* **2022**, *9*, 2106107.
[5] a) D. T. Nguyen, R. Horia, A. Y. S. Eng, S. W. Song, Z. W. Seh, *Mater. Horiz.* **2021**, *8*, 830; b) R. Razaq, P. Li, Y. L. Dong, Y. Li, Y. Mao, S. H. Bo, *EcoMat* **2020**, *2*, e12056; c) H. Ye, Y. Li, *InfoMat* **2022**, *4*, e12291; d) P. Wang, M. R. Buchmeiser, *Adv. Funct. Mater.* **2019**, *29*, 1905248.
[6] a) Y. Song, W. Cai, L. Kong, J. Cai, Q. Zhang, J. Sun, *Adv. Energy Mater.* **2019**, *10*, 1901075; b) Q. Pang, X. Liang, C. Y. Kwok, L. F. Nazar, *Nat. Energy* **2016**, *1*, 16132.
[7] a) Y. You, Y. Ye, M. Wei, W. Sun, Q. Tang, J. Zhang, X. Chen, H. Li, J. Xu, *Chem. Eng. J.* **2019**, *355*, 671; b) J. Wang, D. Luo, J. Li, Y. Zhang, Y. Zhao, G. Zhou, L. Shui, Z. Chen, X. Wang, *Nano Energy* **2020**, *78*, 105293; c) J. Xie, H. J. Peng, Y. W. Song, B. Q. Li, Y. Xiao, M. Zhao, H. Yuan, J. Q. Huang, Q. Zhang, *Angew. Chem., Int. Ed.* **2020**, *59*, 17670.
[8] a) M. Ghidiu, M. R. Lukatskaya, M. Q. Zhao, Y. Gogotsi, M. W. Barsoum, *Nature* **2014**, *516*, 78; b) M. Naguib, V. N. Mochalin, M. W. Barsoum, Y. Gogotsi, *Adv. Mater.* **2014**, *26*, 992; c) X. Liang, A. Garsuch, L. F. Nazar, *Angew. Chem., Int. Ed.* **2015**, *54*, 3907; d) Z. Xiao, Z. Li, P. Li, X. Meng, R. Wang, *ACS Nano* **2019**, *13*, 3608.
[9] H. Kaland, F. Haskjold Fagerli, J. Hadler-Jacobsen, Z. Zhao-Karger, M. Fichtner, K. Wiik, N. P. Wagner, *ChemSusChem* **2021**, *14*, 1864.
[10] a) Z. Li, J. Zhang, X. W. Lou, *Angew. Chem., Int. Ed.* **2015**, *54*, 12886; b) Z. W. Seh, W. Li, J. J. Cha, G. Zheng, Y. Yang, M. T. McDowell, P. C. Hsu, Y. Cui, *Nat. Commun.* **2013**, *4*, 1331; c) H. Wang, T. Zhou, D. Li, H. Gao, G. Gao, A. Du, H. Liu, Z. Guo, *ACS Appl. Mater. Interfaces* **2017**, *9*, 4320; d) Y. Song, W. Zhao, L. Kong, L. Zhang, X. Zhu, Y. Shao, F. Ding, Q. Zhang, J. Sun, Z. Liu, *Energy Environ. Sci.* **2018**, *11*, 2620; e) L. Jiao, C. Zhang, C. Geng, S. Wu, H. Li, W. Lv, Y. Tao, Z. Chen, G. Zhou, J. Li, G. Ling, Y. Wan, Q. H. Yang, *Adv. Energy Mater.* **2019**, *9*, 1900219.
[11] H. Zhang, L. Yang, P. Zhang, C. Lu, D. Sha, B. Yan, W. He, M. Zhou, W. Zhang, L. Pan, Z. Sun, *Adv. Mater.* **2021**, *33*, 2008447.
[12] M. Guo, S. L. Zhong, T. Xu, Y. Q. Huang, G. L. Xia, T. F. Zhang, X. B. Yu, *J. Mater. Chem. A* **2021**, *9*, 23841.
[13] X. Cheng, L. Zu, Y. Jiang, D. Shi, X. Cai, Y. Ni, S. Lin, Y. Qin, *Chem. Commun.* **2018**, *54*, 11622.
[14] a) X. Zheng, M. Yuan, D. Guo, C. Wen, X. Li, X. Huang, H. Li, G. Sun, *ACS Nano* **2022**, *16*, 4487; b) C. Jin, S. S. Rao, J. Xie, Z. T. Sun, J. S.

Gao, Y. Li, B. Li, S. W. Liu, L. Liu, Q. Q. Liu, J. Yang, *Chem. Eng. J.* **2022**, *447*, 137369.

[15] a) H. S. Kim, T. S. Arthur, G. D. Allred, J. Zajicek, J. G. Newman, A. E. Rodnyansky, A. G. Oliver, W. C. Boggess, J. Muldoon, *Nat. Commun.* **2011**, *2*, 427; b) S. Y. Ha, Y. W. Lee, S. W. Woo, B. Koo, J. S. Kim, J. Cho, K. T. Lee, N. S. Choi, *ACS Appl. Mater. Interfaces* **2014**, *6*, 4063; c) Z. Zhao-Karger, X. Zhao, D. Wang, T. Diemant, R. J. Behm, M. Fichtner, *Adv. Energy Mater.* **2015**, *5*, 1401155; d) B. P. Vinayan, Z. Zhao-Karger, T. Diemant, V. S. Chakravadhanula, N. I. Schwarzburger, M. A. Cambaz, R. J. Behm, C. Kubel, M. Fichtner, *Nanoscale* **2016**, *8*, 3296; e) W. Li, S. Cheng, J. Wang, Y. Qiu, Z. Zheng, H. Lin, S. Nanda, Q. Ma, Y. Xu, F. Ye, M. Liu, L. Zhou, Y. Zhang, *Angew. Chem., Int. Ed.* **2016**, *55*, 6406; f) X. Yu, A. Manthiram, *ACS Energy Lett.* **2016**, *1*, 431; g) A. Du, Z. Zhang, H. Qu, Z. Cui, L. Qiao, L. Wang, J. Chai, T. Lu, S. Dong, T. Dong, H. Xu, X. Zhou, G. Cui, *Energy Environ. Sci.* **2017**, *10*, 2616; h) T. Gao, S. Hou, F. Wang, Z. Ma, X. Li, K. Xu, C. Wang, *Angew. Chem., Int. Ed.* **2017**, *56*, 13526; i) A. Robba, A. Vizintin, J. Bitenc, G. Mali, I. Arčon, M. Kavčič, M. Žitnik, K. Bučar, G. Aquilanti, C. Martineau-Corcos, A. Randon-Vitanova, R. Dominko, *Chem. Mater.* **2017**, *29*, 9555; j) Z. Zhang, Z. Cui, L. Qiao, J. Guan, H. Xu, X. Wang, P. Hu, H. Du, S. Li, X. Zhou, S. Dong, Z. Liu, G. Cui, L. Chen, *Adv. Energy Mater.* **2017**, *7*, 1602055; k) Z. Zhao-Karger, M. E. G. Bardaji, O. Fuhr, M. Fichtner, *J. Mater. Chem. A* **2017**, *5*, 10815; l) Z. Zhao-Karger, R. Liu, W. Dai, Z. Li, T. Diemant, B. P. Vinayan, C. Bonatto Minella, X. Yu, A. Manthiram, R. J. Behm, M. Ruben, M. Fichtner, *ACS Energy Lett.* **2018**, *3*, 2005; m) B. P. Vinayan, H. Euchner, Z. Zhao-Karger, M. A. Cambaz, Z. Li, T. Diemant, R. J. Behm, A. Gross, M. Fichtner, *J. Mater. Chem. A* **2019**, *7*, 25490; n) A. Du, Y. Zhao, Z. Zhang, S. Dong, Z. Cui, K. Tang, C. Lu, P. Han, X. Zhou, G. Cui, *Energy Storage Mater.* **2020**, *26*, 23; o) D. Muthuraj, A. Ghosh, A. Kumar, S. Mitra, *ChemElectroChem* **2018**, *6*, 684; p) J. Sun, C. Deng, Y. J. Bi, K. H. Wu, S. M. Zhu, Z. R. Xie, C. L. Li, R. Amal, J. Luo, T. B. Liu, W. Wang, *ACS Appl. Energy Mater.* **2020**, *3*, 2516; q) Y. Xu, G. Zhou, S. Zhao, W. Li, F. Shi, J. Li, J. Feng, Y. Zhao, Y. Wu, J. Guo, Y. Cui, Y. Zhang, *Adv. Sci.* **2020**, *7*, 1903603; r) Q. N. Zhao, R. H. Wang, Y. X. Zhang, G. S. Huang, B. Jiang, C. H. Xu, F. S. Pan, *J. Magnesium Alloys* **2021**, *9*, 78; s) H. Xu, D. Zhu, W. Zhu, F. Sun, J. Zou, R. M. Laine, W. Ding, *Chem. Eng. J.* **2022**, *428*, 131031; t) H. Du, Z. Zhang, J. He, Z. Cui, J. Chai, J. Ma, Z. Yang, C. Huang, G. Cui, *Small* **2017**, *13*, 1702277; u) W. Wang, H. Yuan, Y. NuLi, J. Zhou, J. Yang, J. Wang, *J. Phys. Chem. C* **2018**, *122*, 26764; v) X. Zhou, J. Tian, J. Hu, C. Li, *Adv. Mater.* **2018**, *30*, 1704166; w) Y. Yang, W. Wang, Y. Nuli, J. Yang, J. Wang, *ACS Appl. Mater. Interfaces* **2019**, *11*, 9062; x) X. Zhao, Y. Yang, Y. NuLi, D. Li, Y. Wang, X. Xiang, *Chem. Commun.* **2019**, *55*, 6086.

[16] X. Yang, A. L. Rogach, *Adv. Energy Mater.* **2019**, *9*, 1900747.

[17] B. Lee, J. Choi, S. Na, D.-J. Yoo, J. H. Kim, B. W. Cho, Y.-T. Kim, T. Yim, J. W. Choi, S. H. Oh, *Appl. Surf. Sci.* **2019**, *484*, 933.

[18] a) R. Zhang, C. Cui, R. Xiao, R. Li, T. Mu, H. Huo, Y. Ma, G. Yin, P. Zuo, *Chem. Eng. J.* **2023**, *451*, 138663; b) S. Zhang, W. Ren, Y. NuLi, B. Wang, J. Yang, J. Wang, *Chem. Eng. J.* **2022**, *427*, 130902; c) B. W. Zhang, Y. D. Liu, Y. X. Wang, L. Zhang, M. Z. Chen, W. H. Lai, S. L. Chou, H. K. Liu, S. X. Dou, *ACS Appl. Mater. Interfaces* **2017**, *9*, 24446.